Subakti, Subakti; Daqiqshirazi, Mohammadreza; Wolf, Daniel; Linck, Martin; Kern, Felix L.; Jain, Mitisha; Kretschmer, Silvan; Krasheninnikov, Arkady V.; Brumme, Thomas; Lubk, Axel

Electron holographic mapping of structural reconstruction at mono- and bilayer steps of h-BN

Published in:
Physical Review Research

DOI:
10.1103/PhysRevResearch.5.033137

Published: 01/07/2023

Document Version
Publisher's PDF, also known as Version of record

Please cite the original version:
Subakti, S., Daqiqshirazi, M., Wolf, D., Linck, M., Kern, F. L., Jain, M., Kretschmer, S., Krasheninnikov, A. V., Brumme, T., & Lubk, A. (2023). Electron holographic mapping of structural reconstruction at mono- and bilayer steps of h-BN. *Physical Review Research*, *5*(3), 1-7. Article 033137.
https://doi.org/10.1103/PhysRevResearch.5.033137

PHYSICAL REVIEW RESEARCH **5**, 033137 (2023)

Electron holographic mapping of structural reconstruction at mono- and bilayer steps of *h*-BN

Subakti Subakti,[1] Mohammadreza Daqiqshirazi,[2] Daniel Wolf,[1] Martin Linck,[3] Felix L. Kern,[1] Mitisha Jain,[4]
Silvan Kretschmer,[4] Arkady V. Krasheninnikov,[4,5] Thomas Brumme,[2,*] and Axel Lubk[1,6,†]
[1]*Leibniz Institute for Solid State and Materials Research Dresden, Helmholtzstraße 20, 01069 Dresden, Germany*
[2]*Chair of Theoretical Chemistry, Technische Universität Dresden, Bergstraße 66, 01069 Dresden, Germany*
[3]*Corrected Electron Optical Systems GmbH, Englerstrasse 28, 69126 Heidelberg, Germany*
[4]*Institute of Ion Beam Physics and Materials Research, Helmholtz-Zentrum Dresden-Rossendorf,*
Bautzner Landstraße 400, 01328 Dresden, Germany
[5]*Department of Applied Physics, Aalto University, P.O. Box 11100, FI-00076 Aalto, Finland*
[6]*Institute of Solid State and Materials Physics, Technische Universität Dresden, 01069 Dresden, Germany*

(Received 2 August 2022; revised 4 June 2023; accepted 12 June 2023; published 28 August 2023)

Here, by making use of medium and high resolution autocorrected off-axis electron holography, we directly probe the electrostatic potential as well as in-plane structural reconstruction at edges and steps in multilayer hexagonal boron nitride. In combination with *ab initio* calculations, the data allows revealing the formation of folded zigzag edges at steps comprising two monolayers and their absence at monolayer steps.

DOI: 10.1103/PhysRevResearch.5.033137

I. INTRODUCTION

Two-dimensional (2D) materials consisting of a single or a few atomic layer(s) have been intensively studied for their intriguing chemical and physical properties [1,2]. Particular focus has been put on 2D van der Waals (vdW) materials with a honeycomb lattice such as graphene [3], hexagonal boron nitride (*h*-BN) [4], and transition metal dichalcogenides (TMDCs) [5]. Here, exfoliation allows fabrication of various vdW homo/heterostructures [6], which facilitate band-structure engineering [7,8], proximity-induced exchange coupling [9], or gate tunable photovoltaic devices [10], among other applications.

Despite the fact that graphene has sparked the rapidly growing 2D materials (2DMs) research field, *h*-BN has emerged as a key material for 2D vdW heterostructure building blocks [4,8,11,12]. This mainly derives from its stable honeycomb lattice (in-plane lattice constant 2.504 Å), stabilized by strong in-plane *sp*2-hybridized covalent bonds between alternating boron (B) and nitrogen (N). By virtue of its relatively weak interplanar vdW forces (3.33 Å interplanar distance) it is possible to obtain dangling-bond free exfoliated surfaces as a substrate, as passivation layers, or as insulating layers in the vdW heterostructures [12,13].

Future developments within the field crucially depend on understanding and tailoring the one-dimensional edges and surface steps of 2DMs, because of their unique properties and their prominent role in the 2DMs' chemical and physical properties, such as their mechanical and chemical stability. In the particular case of monolayer honeycomb 2D materials two distinct variants of edges, referred to as zigzag and armchair, exist, which can exhibit very different electronic properties [14,15]. *Ab initio* calculations predict, for instance, that armchair edges of *h*-BN monolayers are insulating and nonmagnetic, whereas zigzag edges are metallic and ferromagnetic. Furthermore, exfoliated 2DMs typically exhibit ripples and wrinkles, crystallographic point and line defects [16], a varying number of stacked layers [17], and stacking layer mismatches, which can also modify the electronic properties. For example, atomically sharp twin boundaries in *h*-BN show conducting behavior with a zero band gap [16]. Similarly, crystallographic point defects can serve as color centers and hence single-photon emitters [18–20] or can be manipulated to control functional properties such as thermoelectricity [21].

Probing and studying these properties requires atomic resolution microscopy techniques, such as scanning probe microscopy techniques, which allow resolving the atomic structure and are sensitive to electronic properties at the same time. Transmission electron microscopy (TEM) based techniques have been successfully used to study freestanding 2DMs including, e.g., defects and edges of freestanding 2DMs [14]. Going one step further, i.e., revealing electronic properties of freestanding edge and step structures with TEM, has proved difficult (see [22] for a notable early exception), mostly because of the small elastic and inelastic

---

[*] thomas.brumme@tu-dresden.de
[†] a.lubk@ifw-dresden.de

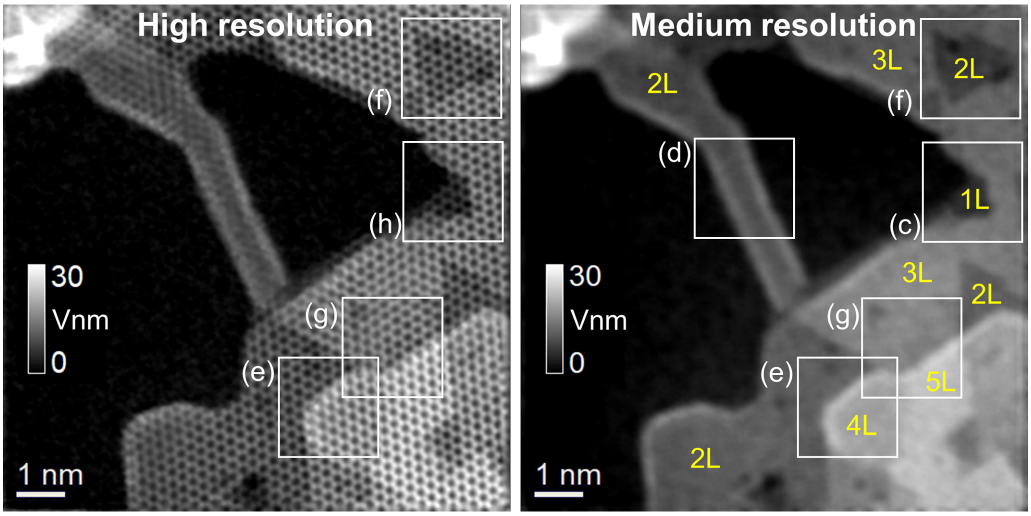

FIG. 1. Atomic-scale (high resolution) and nanometer-scale (medium resolution) projected potential of multilayer *h*-BN reconstructed by off-axis electron holography. The local number of layers is indicated in yellow (e.g., 3 L). The white labeled squares show the regions of interest to be analyzed in detail in Figs. 2(e)–2(h) and Figs. 3(c)–3(g).

scattering cross section of 2DMs. Recently, off-axis holographic and 4D scanning TEM (STEM) techniques have been successfully used to study various 2DMs, exploiting the proportionality between projected electrostatic potential of 2DMs and the phase modulation of the scattered electron wave [23–26].

In Ref. [27], we established how the small elastic scattering cross sections and the ensuing Fourier space symmetries of the scattered electron wave can be exploited to automatically correct for residual aberrations and hence retrieve accurate electrostatic potentials of 2DMs at atomic resolution. Since the electrostatic potential is closely related to the charge density of investigated materials, it is also sensitive to charge redistributions at point defects and nanoscale deformations including corrugated surfaces and wrinkling. In the following, we apply autocorrected off axis holography in combination with *ab initio* calculations to reveal structural and electronic reconstruction at edges and steps of exfoliated multilayers of *h*-BN. We make use of the link between potential and charge density, which is computed by *ab initio* electronic structure calculations, to indirectly reveal the formation of out-of-plane covalent bonds at the zigzag edges of *h*-BN comprising bilayers and the absence of such significant structural and electronic reconstructions in monolayer edges and steps.

II. EXPERIMENTAL AND THEORETICAL METHODS

Thin *h*-BN flakes comprising several multilayers were prepared on a Quantifoil TEM grid using the multistep exfoliation process described in Ref. [14]. Subsequently, the multilayer flake under consideration was further thinned inside the TEM by an electron-beam shower of about 20 nA. This procedure created a terrace landscape of increasingly thinner *h*-BN layers, eventually reaching the monolayer limit (Fig. 1). Utilizing this in-situ thinning in the high vacuum of a TEM column prevented the saturation or decoration of as-prepared steps and edges with foreign atoms, notably hydrogen. Moreover, perfect AB stacking order (i.e., N on top of B) of bulk *h*-BN is preserved within the terraces.

As described in Ref. [27], autocorrected off-axis electron holography allows to quantitatively retrieve projected electrostatic potentials of 2DMs at atomic resolution, exploiting the direct relation between the holographically reconstructed electron wave Ψ and the projected electrostatic potential of the 2DM:

$$\Psi(x, y) = e^{iC_E \int_0^t \Phi(x,y,z)dz}. \tag{1}$$

Here, C_E is an acceleration voltage dependent constant and t denotes the slab thickness containing the potential of the 2DM. The following in-depth analysis of edges and steps in *h*-BN is based on the projected potential dataset reconstructed in Ref. [27] (Fig. 1). Accordingly, we employed the Cs and Cc corrected TEAM I TEM at the Molecular Foundry at the National Berkeley Laboratory to record off-axis holograms at 80 kV acceleration voltage (after thinning the sample). The holograms were acquired under a small defocus of several nanometers (to see the 2DM) as well as residual two- and threefold astigmatism and axial coma. These aberrations were corrected *a posteriori* by an automatic correction algorithm exploiting symmetries of Fourier space phase stemming from the weak phase object property and crystallographic symmetries of *h*-BN. Finally, the obtained projected potentials were denoised by a principal-component denoising algorithm (see [27] for further details on imaging conditions and the reconstruction procedure).

The final projected potential data readily reveals *h*-BN terraces with thicknesses ranging from 1 to 6 monolayers and corresponding edges and steps, which were deliberately generated by the electron beam irradiation in the TEM as described previously. We analyze the projected potential data at two spatial resolutions: the as-reconstructed atomic resolution [Fig. 1(b)] and medium resolution [Fig. 1(a)], where only the average potential per unit cell is considered. The latter was generated from the high-resolution dataset by convolution with a kernel of the size of an *h*-BN unit cell.

The potential averaged over some prismatic volume of base area S and height t (corresponding to sample thickness) defined though

$$\bar{\Phi} = \frac{1}{St}\int_{S\times t} \Phi(\boldsymbol{r})\, d^3 r \tag{2}$$

$$= \sum_n \bar{\Phi}_n \tag{3}$$

can be computed from the sum over average atomic potentials denoted by n, which are obtained from averaging the potential over disjunct subdomains containing only one atom each. As detailed in Refs. [27,28], these averaged atomic potentials may be approximated by the second spatial moments $\langle r_n^2 \rangle = \int \rho_n(\mathbf{r}_n) r_n^2 d^3 r_n$ of the atomic charge densities ρ_n with the subdomain being centered on the atomic core:

$$\bar{\Phi}_n \propto \langle r_n^2 \rangle. \tag{4}$$

Consequently, the averaged potentials serve as a fingerprint for two important charge distribution measures. First, larger densities lead to larger averaged potentials, as larger densities imply smaller disjunct subdomain volumes entering the nominator in the definition of the average atomic potentials. Second, stronger delocalization of the electron shell around the atoms leads to higher second moments and hence higher average potentials. This second contribution is responsible for the significant reduction of the mean inner potential (MIP) of *h*-BN in comparison to graphene, which has a band of delocalized conducting electrons. Moreover, the average projected potential allows to directly count the number of layers (shown in Figs. 1 and 3), which we use to classify the edges and steps into monolayer and bilayer edges and steps (others are not present). Note that all of them terminate in the zigzag structure, which is the energetically favorable configuration in *h*-BN. We generated a set of edge and step zoom-ins facilitating a detailed comparison to first principle calculations, described subsequently.

To describe the mono- and bilayer steps in *h*-BN an all-electron formalism based on density functional theory (DFT) as implemented in FHI-AIMS [29] was employed together with the Perdew-Burke-Ernzerhof (PBE) exchange-correlation functional [30]. Additionally, the van der Waals correction based on the Tkatchenko-Scheffler method [31] was used. All step structures were embedded in supercells comprising 120 atoms, which were relaxed using tight tier-1 numeric atom-centered orbitals until the forces were smaller than 10^{-3} eV/Å and the electron density changed by less than 10^{-6} e/Å. The different steps were simulated employing a supercell geometry with about 60 Å vacuum perpendicular to the layers and 30 Å between the periodically repeated edges. The starting structures prior to relaxation were generated by placing one flat finite *h*-BN monolayer terminating in a zigzag edge over a continuous *h*-BN layer in the case of the monolayer step and a flat finite *h*-BN double layer terminating in a zigzag edge in the case of the bilayer step. The different layers were always stacked in the bulk stacking order (i.e., alternating B and N atoms along z). In the case of the monolayer step, we additionally mirrored the structure in out-of-plane direction in order to avoid the built up of a polarization potential in the otherwise polar step structure. We used a Γ-centered Monkhorst-Pack [32] k-point grid of $13 \times 1 \times 1$ points, and interrupted layers (see results further below) included scalar relativistic corrections (ZORA). For the graphical presentation of the charge density with VMD [33], voxels with a maximum of 0.2 Å edge length were utilized.

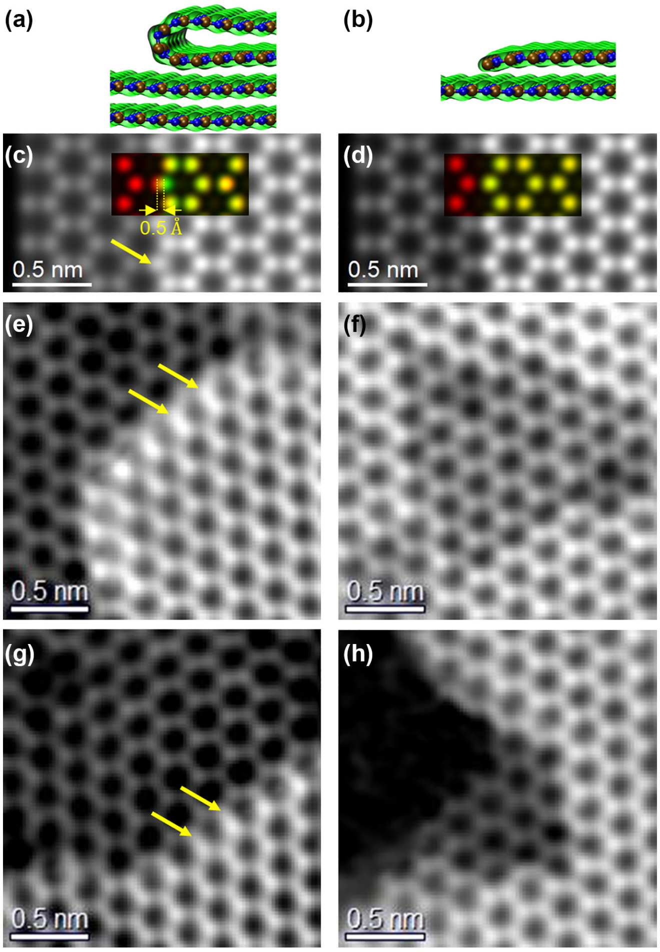

FIG. 2. Simulated and experimental projected potentials of *h*-BN layers at atomic resolution. (a),(b) *Ab initio* relaxed structure (blue: N; brown: B) and electron density (green isodensity surfaces) from DFT calculations for folded bilayer (a) and monolayer (b) steps. (c),(d) Projections of the DFT potentials along the out-of-plane direction for bilayer step (c) and monolayer step (d). The color-coded insets depicting the separately projected bottom (top) layers in red (green) illustrate the lateral shift of the edge atoms at the bilayer step by 0.5 Å (red-green contrast), which is not present at the single layer step (yellow). (e)–(h) Experimental projected potentials of the white squares in Fig. 1 at which (e) and (g) pertain to the folded bilayer step and (f) and (h) to the monolayer step.

In order to verify whether dynamical scattering effects produce a deviation of the scattered electron's wave function phase from the projected electrostatic potential [i.e., the relationship described by Eq. (1)], we carried out multislice (i.e., split operator) dynamic scattering simulations employing the SEMI scattering simulation package [34] (lateral sampling

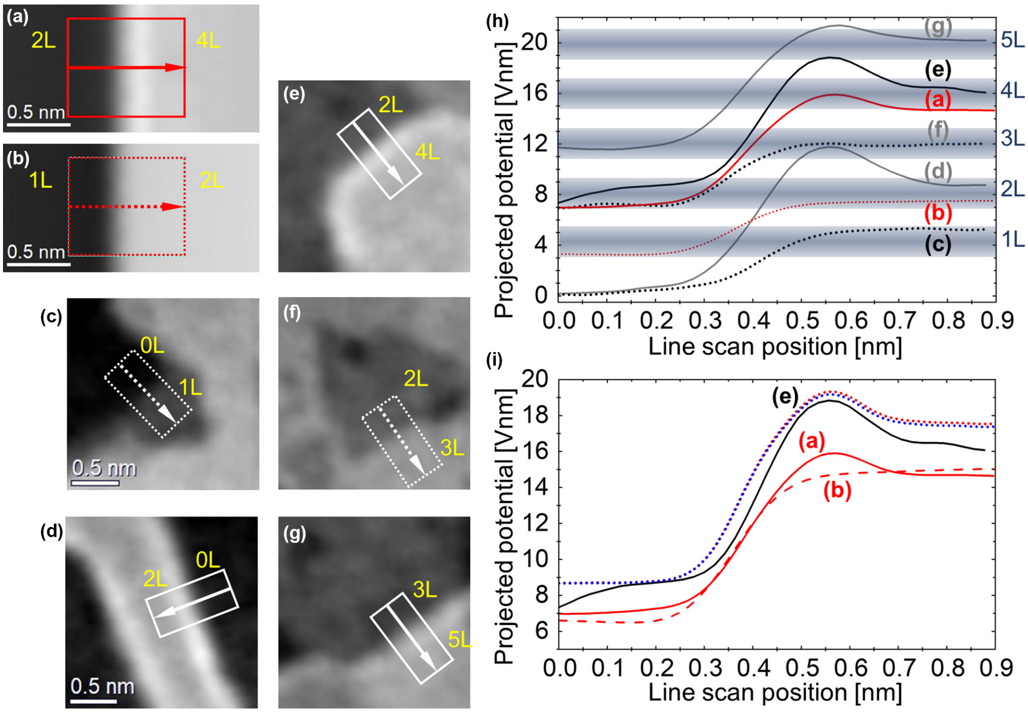

FIG. 3. Nanoscale projected potentials of *h*-BN mono- and bilayer steps. (a),(b) Projected DFT potential corresponding to Figs. 2(a) and 2(b). (c)–(g) Zoomed-in views of the experimental medium resolution potentials indicated by white squares in Fig. 1. The number of monolayers L are indicated. (h) Line profiles pertaining to arrows in (a)–(g), where the rectangles illustrate the integration width perpendicular to the scan direction. Theoretical and experimental data are plotted in red and black or gray, respectively. The line profiles of the bilayer (monolayer) steps are plotted as solid (dashed) lines. The number of layers is visualized as gray-blue bands to account for experimental uncertainties (e.g., slight charging, instabilities). (i) Potential profiles of the 2L–4L step as shown in (h) with profiles from isolated atom potentials placed at relaxed positions either obtained by simple projection (dotted blue) or by scattering simulations (dotted red). The dashed red line (b) is two times the potential change of the single layer step for comparison.

0.01 Å, integration step size 0.1 Å), using the experimental microscope parameters (80 kV acceleration voltage, incoherent envelope defined by image spread [27]).

To understand the morphology of the edges of *h*-BN sheets under the experimental conditions and to assess whether surface decoration by hydrogen atoms has to be considered in the interpretation of the results, the displacement rates of atoms under the electron beam were assessed using the DFT-based molecular dynamics (MD) and the McKinley-Feshbach formalism [35], as done previously for various 2D materials [36]. The DFT-MD simulations were carried out using the Vienna Ab initio Simulation Package (VASP) [37–40]. The Perdew-Burke-Ernzerhof (PBE) exchange-correlation functional was used [41]. The edge of *h*-BN sheet was modeled as a *h*-BN ribbon with a width of about 16 Å. The dangling bonds at the edges of the ribbon were saturated with hydrogen atoms. The periodic images of the supercell were separated by 9 Å in the in-plane direction and by 40 Å in the transverse directions. A tight energy convergence (10^{-5} eV) criterion was used for electronic steps on a $1 \times 1 \times 1$ Γ-centered k-point mesh. The cutoff energy was set to 400 eV and a time step of 0.1 fs was employed. Mimicking the impacts of energetic electrons, initial kinetic energy was instantaneously assigned to the recoil atom. The atom was assumed to be displaced if it is moved by 4 Å or more, and the initial kinetic energy of the atom was taken as the threshold energy.

III. RESULTS

Figures 2(a) and 2(b) depict structures of bilayer and monolayer steps as predicted by DFT, respectively, together with simulated and experimental high-resolution potential distributions at steps and edges comprising one (right column) or two layer(s) (left column).

Most notably, the simulated structure of the bilayer step exhibits a strong deformation of the terminating edge structure. The terminating bilayers are bent such that they mutually interconnect at the step by forming an out-of-plane covalent bond (indicated by green isocharge surfaces extending to connect both layers). That out-of-plane reconstruction implies a small in-plane reduction/compression of the interatomic distances by 0.5 Å at the edge, as shown in Fig. 2(c). This strong deformation of the layers is not present in the simulated single step structure Fig. 2(d). Our *ab initio* calculations, however, also show the formation of conducting states at the monolayer step similar to those obtained for the monolayer zigzag edge [42]). Furthermore, Bader charge analysis of the DFT results also indicates a mixed covalent-ionic character of the BN bond similar to Ref. [43], which gets also modified at the edges. Subsequently, we conduct a detailed comparison of *ab initio* simulation and experiment to verify (i) the reconstruction at the bilayer *h*-BN steps, and (ii) how the holographic potential data reflects this reconstruction.

The high-resolution datasets indicate the in-plane structural changes (i.e., in-plane shift of the atomic positions) pertaining to the folded bilayer and nonfolded monolayer steps. Projected potentials of bilayer steps exhibit a subtle mutual lateral shift of the terminating atoms in adjacent *h*-BN layers visible by a smeared contrast indicated by yellow arrows in both the simulation [Fig. 2(c)] and the experiment [Figs. 2(e) and 2(g)] that are not present at monolayer steps [Figs. 2(d), 2(f), and 2(h)]. The presence of these shifts in the bilayer step may be explained by the loss of perfect stacking of adjacent layers due to the previously noted deformation of the bilayer step. Note, however, that while this observation indicates a difference between mono- and bilayer steps, the effect is too weak to corroborate the predicted presence of the folded bilayer step, i.e., the reconstruction in both in-plane and out-of-plane directions.

In the unit-cell-wise averaged DFT potentials (Figs. 1 and 3), the structural reconstruction manifests in a twofold way. First, the in-plane shift of the terminating row of atoms corresponds to a subtle in-plane compression of the upper two layers at the edge, and hence an increase of the averaged potential at the edge/step. Second, the formation of a covalent bond between *sp*2 orbitals of terminating B and N atoms of the adjacent layers at the edge, as visible through the continuous electron density isosurface in Fig. 2(a), implies a subtle delocalization of electrons, which also leads to an increase of the simulated average projected potential of the bilayer step [Fig. 3(a)]. Both effects are absent in the monolayer step [Fig. 3(b)].

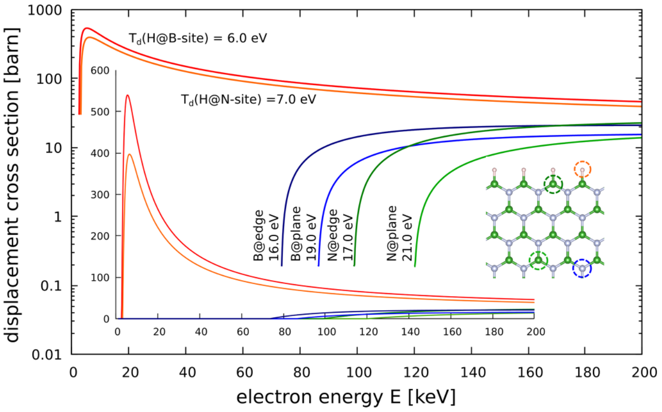

FIG. 4. Electron energy dependent displacement cross sections for H/B/N atoms displaced from *h*-BN ribbons. For better comparability, the ordinate scale on the main plot is logarithmic; the inset shows the linear scale. The inset image on the right illustrates the different target sites for the nitrogen terminated zigzag edge. Predominantly hydrogen atoms will be sputtered such that the edge will quickly become "naked."

Indeed, the holographically reconstructed averaged projected potentials agree very well with that theoretically predicted behavior. The bilayer steps and edges exhibit a systematic increase of the potential at the edge [Fig. 3(e), 3(d), and 3(g)], which is not present at the monolayer steps and edges [Figs. 3(c) and 3(f); see also potential profiles in Fig. 3(h)]. Here we abstain from a discussion of differences between 1–3, 2–4, and 3–5 steps, as the experimental database was too small to draw significant conclusions about the differences. To find out whether the lateral shift or the out-of-plane electron delocalization is the main source of the observed potential increase, we additionally calculate the projected potential from independent atomic potentials (parameterization due to Weickenmeier and Kohl [44]) being placed at the relaxed positions of the bilayer step [Fig. 2(a)]. These independent atomic potentials do not contain any increase from delocalized charge densities (chemical bonds). The occurrence of the potential bump in the projected potential created from independent atoms at the edge and its agreement with the experimental data indicates that the structural lateral shift of the atoms (i.e., in-plane compression of the structure) at the edge is the main source of the potential increase at the bilayer step. The observed offset of the independent atom average potentials to the DFT and experimental potentials stems from the systematically larger delocalization of the electron shell of independent atoms not incorporated into a crystal lattice with chemical bonds. In Ref. [27] we found almost perfect agreement between the averaged DFT and holographic potentials in the thicker regions of the sample. The apparently better match of the experimental potentials close to the edges to the higher MIP obtained from independent atomic potentials can be associated to slightly positive charging of the sample in the electron beam, which cannot be avoided in insulating *h*-BN. Note furthermore that a full dynamic scattering simulation [Fig. 3(i)] carried out at the bilayer step structure populated with independent atomic potentials yields almost the same phase shift, corroborating the weak (scattering) phase object character of the few layer *h*-BN.

We can furthermore exclude that the potential increase originates from a systematic decoration/saturation by foreign atoms, in particular hydrogen, because of the previously noted *in vacuo* preparation of the samples.

Moreover, our DFT-MD simulations indicate that even if the edges were decorated by H atoms, they would have been quickly sputtered away by the electron beam. To prove that, we carried out DFT-MD simulations, as described above, and obtained the following threshold displacement energies for H, B, and N atoms: For B and N atoms in the pristine *h*-BN structure, the threshold energies were found to be $T_d^B = 19\,\text{eV}$ and $T_d^N = 21\,\text{eV}$, which are close to the earlier calculated values [45]. Much smaller values of $\sim 6/7\,\text{eV}$ were obtained for H atoms at B and N atoms. For the sake of completeness, displacement thresholds were also computed for B and N atoms at the edges.

The cross sections calculated using these displacement energies and employing the McKinley-Feshbach formalism are presented in Fig. 4. It is evident that, in the whole range of energies studied, the probability of displacing H atom saturating dangling bonds at the edges of *h*-BN flakes is much higher than the probability of displacing a B or N atom from the edges or the bulk of the system. Thus, even if the edges of *h*-BN flakes were saturated with H atoms, the edges would have been very quickly become "naked."

Consequently, the information encoded in the medium resolution projected potential data provides evidence for the strong structural reconstruction in the folded bilayer *h*-BN step. The monolayer step/edge, on the other hand, does not exhibit such a strong structural reconstruction and hence potential increase [Fig. 3(j)].

IV. SUMMARY

We demonstrated that the combination of holographically reconstructed projected potentials and *ab initio* calculations allows indirect reconstruction of *h*-BN structural edges. Holographically reconstructed medium- and high-resolution projected potential data combined with *ab initio* calculations of bilayer steps in *h*-BN revealed the formation of stitched edges consisting of in-plane compression and out-of-plane deformation of two adjacent layers steps, which is not the case for single-layer steps. Since the edge step reconstruction already leads to clearly visible changes in the averaged or mean inner potential, the results suggest that holographic experiments at medium resolution performed in conventional TEMs are sufficient for the analysis of structural and electronic properties of 2DMs. In particular, this includes the study of edge-termination and interlayer-step reconstructions in various other 2DMs as well as their defects.

ACKNOWLEDGMENTS

The authors acknowledge funding from DFG SFB 1415, Project ID No. 417590517. We thank the Center for Information Services and High-Performance Computing (ZIH) at TU Dresden for generous allocations of computer time. The authors gratefully acknowledge the Gauss Centre for Supercomputing e.V. [46] for funding this project by providing computing time through the John von Neumann Institute for Computing (NIC) on the GCS Supercomputer JUWELS [47] at Jülich Supercomputing Centre (JSC). We further thank HLRS, Stuttgart, Germany, and TU Dresden Cluster "Taurus" for generous grants of CPU time.

---

[1] S. Das, A. Sebastian, E. Pop, C. J. McClellan, A. D. Franklin, T. Grasser, T. Knobloch, Y. Illarionov, A. V. Penumatcha, J. Appenzeller, Z. Chen, W. Zhu, I. Asselberghs, L. J. Li, U. E. Avci, N. Bhat, T. D. Anthopoulos, and R. Singh, Transistors based on two-dimensional materials for future integrated circuits, Nat. Electron. **4**, 786 (2021).

[2] H. Li, X. Jia, Q. Zhang, and X. Wang, Metallic transition-metal dichalcogenide nanocatalysts for energy conversion, Chem **4**, 1510 (2018).

[3] K. S. Novoselov, A. K. Geim, S. V. Morozov, D. Jiang, Y. Zhang, S. V. Dubonos, I. V. Grigorieva, and A. A. Firsov, Electric field in atomically thin carbon films, Science **306**, 666 (2004).

[4] K. Zhang, Y. Feng, F. Wang, Z. Yang, and J. Wang, Two dimensional hexagonal boron nitride (2D-hBN): Synthesis, properties and applications, J. Mater. Chem. C **5**, 11992 (2017).

[5] S. Manzeli, D. Ovchinnikov, D. Pasquier, O. V. Yazyev, and A. Kis, 2D transition metal dichalcogenides, Nat. Rev. Mater. **2**, 17033 (2017).

[6] A. K. Geim and I. V. Grigorieva, Van der Waals heterostructures, Nature (London) **499**, 419 (2013).

[7] F. Withers, O. Del Pozo-Zamudio, A. Mishchenko, A. P. Rooney, A. Gholinia, K. Watanabe, T. Taniguchi, S. J. Haigh, A. K. Geim, A. I. Tartakovskii, and K. S. Novoselov, Light-emitting diodes by band-structure engineering in van der Waals heterostructures, Nat. Mater. **14**, 301 (2015).

[8] K. Nakamura, N. Nagamura, K. Ueno, T. Taniguchi, K. Watanabe, and K. Nagashio, All 2D heterostructure tunnel field-effect transistors: Impact of band alignment and heterointerface quality, ACS Appl. Mater. Interfaces **12**, 51598 (2020).

[9] K. Zollner, P. E. Faria Junior, and J. Fabian, Giant proximity exchange and valley splitting in transition metal dichalcogenide/*h*BN/(Co,Ni) heterostructures, Phys. Rev. B **101**, 085112 (2020).

[10] N. Flöry, A. Jain, P. Bharadwaj, M. Parzefall, T. Taniguchi, K. Watanabe, and L. Novotny, A $WSe_2/MoSe_2$ heterostructure photovoltaic device, Appl. Phys. Lett. **107**, 2 (2015).

[11] S. Zheng, M. Zhao, L. Sun, and H. Yang, Classical and quantum phases in hexagonal boron nitride-combined van der Waals heterostructures, InfoMat **3**, 252 (2021).

[12] S. Roy, X. Zhang, A. B. Puthirath, A. Meiyazhagan, S. Bhattacharyya, M. M. Rahman, G. Babu, S. Susarla, S. K. Saju, M. K. Tran, L. M. Sassi, M. A. Saadi, J. Lai, O. Sahin, S. M. Sajadi, B. Dharmarajan, D. Salpekar, N. Chakingal, A. Baburaj, X. Shuai *et al.*, Structure, properties and applications of two-dimensional hexagonal boron nitride, Adv. Mater. **33**, 2101589 (2021).

[13] J. Wang, F. Ma, and M. Sun, Graphene, hexagonal boron nitride, and their heterostructures: Properties and applications, RSC Adv. **7**, 16801 (2017).

[14] N. Alem, R. Erni, C. Kisielowski, M. D. Rossell, W. Gannett, and A. Zettl, Atomically thin hexagonal boron nitride probed by ultrahigh-resolution transmission electron microscopy, Phys. Rev. B **80**, 155425 (2009).

[15] A. Yamanaka and S. Okada, Polarity control of h-BN nanoribbon edges by strain and edge termination, Phys. Chem. Chem. Phys. **19**, 9113 (2017).

[16] H. J. Park, J. Cha, M. Choi, J. H. Kim, R. Y. Tay, E. H. T. Teo, N. Park, S. Hong, and Z. Lee, One-dimensional hexagonal boron nitride conducting channel, Sci. Adv. **6**, eaay4958 (2020).

[17] S. M. Gilbert, T. Pham, M. Dogan, S. Oh, B. Shevitski, G. Schumm, S. Liu, P. Ercius, S. Aloni, M. L. Cohen, and A. Zettl, Alternative stacking sequences in hexagonal boron nitride, 2D Mater. **6**, 021006 (2019).

[18] D. Yim, M. Yu, G. Noh, J. Lee, and H. Seo, Polarization and localization of single-photon emitters in hexagonal boron nitride wrinkles, ACS Appl. Mater. Interfaces **12**, 36362 (2020).

[19] M. Fischer, J. M. Caridad, A. Sajid, S. Ghaderzadeh, M. Ghorbani-Asl, L. Gammelgaard, P. Bøggild, K. S. Thygesen, A. V. Krasheninnikov, S. Xiao, M. Wubs, and N. Stenger, Controlled generation of luminescent centers in hexagonal boron nitride by irradiation engineering, Sci. Adv. **7**, eabe7138 (2021).

[20] W. F. Koehl, B. B. Buckley, F. J. Heremans, G. Calusine, and D. D. Awschalom, Room temperature coherent control of defect spin qubits in silicon carbide, Nature (London) **479**, 84 (2011).

[21] J. Wu, Y. Liu, Y. Liu, Y. Cai, Y. Zhao, H. K. Ng, K. Watanabe, T. Taniguchi, G. Zhang, C. W. Qiu, D. Chi, A. H. Castro Neto, J. T. Thong, K. P. Loh, and K. Hippalgaonkar, Erratum: Large enhancement of thermoelectric performance in $\mathrm{MoS_2}$/h-BN heterostructure due to vacancy-induced band hybridization [Proc Natl. Acad. Sci. U.S.A. 117, 13929 (2020)], Proc. Natl. Acad. Sci. U.S.A. **117**, 18127 (2020).

[22] N. Alem, Q. M. Ramasse, C. R. Seabourne, O. V. Yazyev, K. Erickson, M. C. Sarahan, C. Kisielowski, A. J. Scott, S. G. Louie, and A. Zettl, Subangstrom Edge Relaxations Probed by Electron Microscopy in Hexagonal Boron Nitride, Phys. Rev. Lett. **109**, 205502 (2012).

[23] L. Ortolani, F. Houdellier, M. Monthioux, E. Snoeck, and V. Morandi, Surface electrostatic potentials in carbon nanotubes and graphene membranes investigated with electron holography, Carbon **49**, 1423 (2011).

[24] D. Cooper, C.-T. Pan, and S. Haigh, Atomic resolution electrostatic potential mapping of graphene sheets by off-axis electron holography, J. Appl. Phys. **115**, 233709 (2014).

[25] F. Winkler, J. Barthel, A. H. Tavabi, S. Borghardt, B. E. Kardynal, and R. E. Dunin-Borkowski, Absolute Scale Quantitative Off-Axis Electron Holography at Atomic Resolution, Phys. Rev. Lett. **120**, 156101 (2018).

[26] S. Fang, Y. Wen, C. S. Allen, C. Ophus, G. G. Han, A. I. Kirkland, E. Kaxiras, and J. H. Warner, Atomic electrostatic maps of 1D channels in 2D semiconductors using 4D scanning transmission electron microscopy, Nat. Commun. **10**, 1127 (2019).

[27] F. Kern, M. Linck, D. Wolf, N. Alem, H. Arora, S. Gemming, A. Erbe, A. Zettl, B. Büchner, and A. Lubk, Autocorrected off-axis holography of two-dimensional materials, Phys. Rev. Res. **2**, 043360 (2020).

[28] M. O'Keeffe and J. C. Spence, On the average Coulomb potential ($\Sigma 0$) and constraints on the electron density in crystals, Acta Crystallogr. A **50**, 33 (1994).

[29] V. Blum, R. Gehrke, F. Hanke, P. Havu, V. Havu, X. Ren, K. Reuter, and M. Scheffler, Ab initio molecular simulations with numeric atom-centered orbitals, Comput. Phys. Commun. **180**, 2175 (2009).

[30] J. P. Perdew, K. Burke, and M. Ernzerhof, Generalized Gradient Approximation Made Simple, Phys. Rev. Lett. **77**, 3865 (1996).

[31] A. Tkatchenko and M. Scheffler, Accurate Molecular Van Der Waals Interactions from Ground-State Electron Density and Free-Atom Reference Data, Phys. Rev. Lett. **102**, 073005 (2009).

[32] H. J. Monkhorst and J. D. Pack, Special points for Brillouin-zone integrations, Phys. Rev. B **13**, 5188 (1976).

[33] W. Humphrey, A. Dalke, and K. Schulten, VMD: Visual molecular dynamics, J. Mol. Graphics **14**, 33 (1996).

[34] A. Lubk, *Paraxial Quantum Mechanics, in Advances in Imaging and Electron Physics*, Vol. 206 (Elsevier, Amsterdam, 2018), Chap. 2, pp. 15–58.

[35] W. A. McKinley and H. Feshbach, The coulomb scattering of relativistic electrons by nuclei, Phys. Rev. **74**, 1759 (1948).

[36] J. C. Meyer, F. Eder, S. Kurasch, V. Skakalova, J. Kotakoski, H. J. Park, S. Roth, A. Chuvilin, S. Eyhusen, G. Benner, A. V. Krasheninnikov, and U. Kaiser, Accurate Measurement of Electron Beam Induced Displacement Cross Sections for Single-Layer Graphene, Phys. Rev. Lett. **108**, 196102 (2012).

[37] G. Kresse and J. Hafner, *Ab initio* molecular dynamics for liquid metals, Phys. Rev. B **47**, 558 (1993).

[38] G. Kresse and J. Furthmüller, Efficiency of ab-initio total energy calculations for metals and semiconductors using a plane-wave basis set, Comput. Mater. Sci. **6**, 15 (1996).

[39] G. Kresse and J. Furthmüller, Efficient iterative schemes for ab initio total-energy calculations using a plane-wave basis set, Phys. Rev. B **54**, 11169 (1996).

[40] G. Kresse and D. Joubert, From ultrasoft pseudopotentials to the projector augmented-wave method, Phys. Rev. B **59**, 1758 (1999).

[41] J. P. Perdew, K. Burke, and M. Ernzerhof, Erratum: Generalized Gradient Approximation Made Simple [Phys. Rev. Lett. 77, 3865 (1996)], Phys. Rev. Lett. **78**, 1396(E) (1997).

[42] V. Barone and J. E. Peralta, Magnetic boron nitride nanoribbons with tunable electronic properties, Nano Lett. **8**, 2210 (2008).

[43] S. Yamamura, M. Takata, and M. Sakata, Charge density of hexagonal boron nitride using synchrotron radiation powder data by maximum entropy method, J. Phys. Chem. Solids **58**, 177 (1997).

[44] A. Weickenmeier and H. Kohl, Computation of absorptive form factors for high-energy electron diffraction, Acta Crystallogr. A **47**, 590 (1991).

[45] J. Kotakoski, C. H. Jin, O. Lehtinen, K. Suenaga, and A. V. Krasheninnikov, Electron knock-on damage in hexagonal boron nitride monolayers, Phys. Rev. B **82**, 113404 (2010).

[46] http://www.gauss-centre.eu.

[47] Jülich Supercomputing Centre, JUWELS Cluster and Booster: Exascale pathfinder with modular supercomputing architecture at Juelich Supercomputing Centre, J. Large-Scale Res. Facilities **7**, A183 (2021).